A TCAD-based modeling of GaN/InGaN/Si solar cells

A TCAD-based modeling of GaN/InGaN/Si solar cells

Muhammad Nawaz[1,3] and Ashfaq Ahmad[2]

[1] University Graduate Centre (UNIK), Gunnar Randers Vei 19, P. O. Box 70, NO-2027 Kjeller, Norway
[2] COMSATS Institute of Information Technology, Off-Raiwind Road, Lahore-54000, Pakistan

E-mail: Muhammad.Nawaz@se.abb.com

Abstract

Theoretical efficiency potential of GaN/InGaN/cSi tandem solar cells is investigated using two-dimensional numerical computer simulation (i.e. technology-based computer aided design tool: TCAD). With double-junction GaN/InGaN/cSi tandem design, a conversion efficiency of 27% is achieved using a 1.0 μm $In_{0.5}Ga_{0.5}N$ absorber of top cell over crystalline silicon (cSi) bottom cell. This efficiency is further improved to 29.0% with grading of the $In_xGa_{1-x}N$ absorber layer close to the top heterointerface (p^+-GaN/n^--$In_xGa_{1-x}N$) of the solar cell. A maximum conversion efficiency is obtained when the band discontinuity ratio (i.e. ΔE_C:ΔE_V) is set to 0.65:0.35. While efficiency remains approximately constant with moderate n-doping (up to 5 $\times$ 10^{16} cm^{-3}) in the top InGaN absorber layer, sensitivity of the efficiency to the interface trap density and trap cross-section (when traps are located only at the heterointerfaces) shows degraded behavior with increasing trap density and trap cross-section. A temperature coefficient for open-circuit voltage (efficiency) of -0.15 (-1.72×10^{-3} °C^{-1}), -0.09 (-0.95×10^{-3} °C^{-1}) and -0.2 (-2.38×10^{-3} °C^{-1})%/°C for single heterojunction (SHJ), double-heterojunction (DHJ) and tandem-graded design is predicted from the numerical simulations.

(Some figures may appear in colour only in the online journal)

1. Introduction

Rapid progress in III-N (nitride) material growth and device fabrication has enabled demonstration of UV light-emitting diodes with emission from 200 nm to 400 nm [1–3] and high-efficiency visible-blind and solar-blind photodetectors [4, 5] for commercial and military applications. Since the application area of the III-nitride devices is steadily spreading, several new commercial devices such as UV-LED and high-frequency high-power electronic devices begin to be available.

An earlier effort on more traditional double- and triple-junction tandem design using III–V alloys (and Ge) has shown a record efficiency of over 30% [6] and of 41.6% [7], respectively, using solar concentrators. Recently, the potential of using III-N material for photovoltaic application [8–14] has been explored through various device configurations such as InGaN/GaN multiple quantum well solar cells

on sapphire substrate [9], plasmonic nanoparticles on p-GaN/InGaN/GaN quantum wells for enhanced photocurrent on sapphire substrate [8] and GaN/silicon first tandem solar cells on silicon substrate [10]. A first proof of concept has demonstrated using a pn-GaN/AlN-buffer/pn-Si tandem structure showing an open-circuit voltage (V_{OC}) of 2.4 V and an efficiency of 1.5% [10]. A multiple quantum well (MQW)-based solar cell structure composed of 10 periods of $In_xGa_{1-x}N$/GaN on Si substrate with sandwiched n-type doped 100 nm SiCN (*silicon carbon nitride)* buffer layer has shown a conversion efficiency of 38.5% under air mass 1.5 solar spectrum [11]. In fact, the use of a thin SiCN buffer layer reduces the lattice mismatch of Si with GaN that leads to fewer problems with defects generation and dislocations [11].

With superior material characteristics (i.e. direct bandgap in the entire alloy range, high carrier mobility, high drift velocity, radiation resistance and optical absorption $>10^5$ cm^{-1}), InGaN alloy as an active absorber material covers almost the whole solar spectrum due to its wide bandgap tunability from 3.42 eV (i.e. GaN) to 0.7 eV (i.e.

[3] Corresponding address: ABB Corporate Research, Forskargränd 7, SE-72178 Västerås, Sweden.
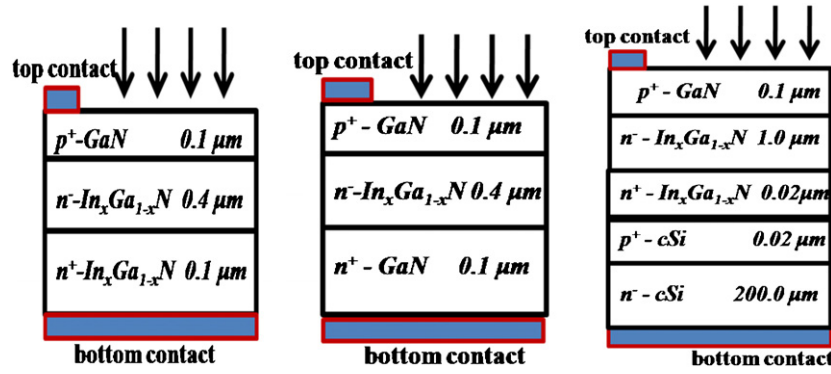
Figure 1. Schematic layer structures (left is single heterojunction SHJ, middle is double heterojunction DHJ, right is double-junction tandem design with top InGaN and bottom Si component cell) used in the device simulation.

InN). A tandem-type solar cell design with the usage of $In_xGa_{1-x}N$ over Si therefore offers some advantages such as the availability of required bandgap for better current matching of the two component cells, and the formation of low resistance tunnel junction at the n^+-$In_xGa_{1-x}N/p^+$-cSi interface since the conduction band of $In_xGa_{1-x}N$ (for In content of ∼0.45–0.5) has the same energy (relative to the vacuum level) as the valence band of Si [12]. Development of InGaN solar cells on silicon substrate [10, 11] with efficiency potential comparable to that of more traditional III–V based costly solar cell alternatives presents therefore a more favorable choice. Earlier simple analytical calculations have predicted a conversion efficiency of 31% [12] for pn-InGaN/pn-Si cells and more recently of 28.9% [14] using finite element analysis for double-junction $In_xGa_{1-x}N$/cSi tandem solar cells.

The purpose of this paper is to assess the efficiency potential of p^+-GaN/n^--InGaN/n^+-InGaN-based single heterojunction (SHJ), p^+-GaN/n^--InGaN/n^+-GaN-based double heterojunction (DHJ) and p^+-GaN/n^--InGaN/n^+-InGaN/p^+-cSi/n^--cSi-based tandem cells by varying indium content of the top cell, bandgap distribution of the top cell, doping of the top absorber and by inserting traps at the semiconductor interface between bottom Si and top InGaN component cells. These design parameters have been studied using two-dimensional numerical computer simulation (i.e. TCAD using ATLAS from Silvaco) [15] using physical device simulation which not only provides better physics insight but also realistic predictive capability.

2. Computer model

Solar cell structures used in the device simulation are shown in figure 1. Aluminum (Al) is used as the top and back metal contact layers. First SHJ based on the p^+-GaN/n^--InGaN/n^+-InGaN system and DHJ based on the p^+-GaN/n^--InGaN/n^+-GaN material system in p–i–n-type configuration are analyzed to assess the dependences of the efficiency on the indium content and layer thicknesses. Tandem design is based on the top component cell using the p^+-GaN/n^--$In_xGa_{1-x}N/n^+$-$In_xGa_{1-x}N$ system and the bottom component cell using p^+-cSi/n^--cSi (i.e. crystalline silicon). A tandem-graded design (a subset of tandem design not shown here due to similarity) is also explored which is based on the top

component cell using the p^+-GaN/n^--graded-$In_xGa_{1-x}N/n^-$-$In_xGa_{1-x}N/n^+$-$In_xGa_{1-x}N$ system and the bottom component cell using the p^+-cSi/n^--cSi (i.e. crystalline silicon). Only the top portion of 50 nm range close to the top p^+-GaN/n^--$In_xGa_{1-x}N$ heterojunction is graded inside the InGaN absorber with varying indium content from 0 to 0.5 (i.e. decreasing band gap of InGaN from the top heterointerface) to eliminate the valence band potential discontinuity (see band diagram figure 3(d)). The rest of the top InGaN absorber (and the whole structure) in the tandem-graded design remains the same as tandem design (figure 1: right). For all cases, the doping of the top p^+-GaN layer is set at 5×10^{18} cm^{-3}. The doping of the bottom n^+-GaN and n^+-$In_xGa_{1-x}N$ layers for DHJ and SHJ, respectively, is set at 1×10^{19} cm^{-3}. For tandem design, the doping of the n-type Si wafer is assumed to be 5×10^{15} cm^{-3} and p^+-cSi layer is set to 1×10^{19} cm^{-3}. A general expression for the wavelength-dependent absorption coefficient [14] of $In_xGa_{1-x}N$ used in the simulation is given as

$$\alpha(\text{cm}^{-1}) = 1.0 \times 10^5 \cdot [C \cdot (E_{ph} - E_g) + D \cdot (E_{ph} - E_g)^2]^{1/2}$$
(1)

where E_{ph} is the photon energy, C and D are composition-dependent parameters given elsewhere [14] for $In_xGa_{1-x}N$. Earlier, equation (1) has been used to get best fit with experimental data of absorption coefficient of InGaN material [17]. E_g is the composition-dependent energy bandgap of $In_xGa_{1-x}N$ (at room temperature) which is calculated as follows:

$$E_{gInGaN} = xE_{gInN} + (1-x)E_{gGaN} - b \cdot x \cdot (1-x)$$
(2)

where x is the indium content, $E_{gInN} = 0.7$ eV [16], $E_{gGaN} = 3.42$ eV [16] and bowing parameter b is 1.43 [16]. Other modeling parameters such as permittivity ($\varepsilon/\varepsilon_o$) [15], affinity ($\chi$) [15] and effective masses (m_e/m_h) [15] are calculated as follows:

$$\varepsilon(In_xGa_{1-x}N) = 15.3x + 8.9(1-x)$$
(3)

$$\chi(In_xGa_{1-x}N) = 3.659x - 2.666x^2 + 4.31$$
(4)

$$m_e(In_xGa_{1-x}N) = 0.12x + 0.2(1-x)$$
(5)

$$m_h(In_xGa_{1-x}N) = 0.17x + 1.0(1-x).$$
(6)

The wavelength-dependent refractive index model of Adachi given in [15] is used for $In_xGa_{1-x}N$ as follows:

$$n(E) = [A \cdot (E_{ph}/E_g)^{-2} \cdot \{2 - (1 + E_{ph}/E_g)^{0.5} - (1 - E_{ph}/E_g)^{0.5}\} + B]^{0.5} \quad (7)$$

where $A(In_xGa_{1-x}N) = 13.55x + 9.31(1-x)$ and $B(In_xGa_{1-x}N) = 2.05x + 3.03(1-x)$.

A general expression (as shown below) for low field mobility developed earlier by M Farahmand *et al* [18] is used for electron and hole mobilities of III-nitride materials:

$$\mu_o(N, T) = \mu_{min,i} \left[\frac{T}{300} \right]^{\beta 1} + \frac{(\mu_{max,i} - \mu_{min,i}) \left[\frac{T}{300} \right]^{\beta 2}}{1 + \left[\frac{N}{N_{ref} \left(\frac{T}{300} \right)^{\beta 3}} \right]^{\gamma \left(\frac{T}{300} \right)^{\beta 4}}} \quad (8)$$

where N is the doping concentration, N_{ref} is fixed at 1×10^{17} cm^{-3}, T is the temperature, β_1, β_2, β_3, β_4 and γ are specific parameters for a given material [18]. For GaN, μ_{max} and μ_{min} values for electron (hole) mobility are 1460 (170) and 295 (5) cm^2 V$^{-1} \cdot$ s^{-1} [18, 19] respectively. Similarly, μ_{max} and μ_{min} values are 3138 (340) and 774 (15) cm^2 V$^{-1} \cdot$ s^{-1} [18, 19], respectively, for electrons (holes) for InN material. Using these data, $\mu_o(N, T)$ is first calculated for GaN and InN material and mobilities for InGaN are then linearly interpolated for electrons and holes as follows:

$$\mu_n(In_xGa_{1-x}N) = 524x + \mu_n(GaN) \quad (9)$$

$$\mu_h(In_xGa_{1-x}N) = 6.5x + \mu_h(GaN). \quad (10)$$

Temperature dependence of the bandgap is taken into account using the following expression [15]:

$$E_g(T) = E_{g300}(In_x Ga_{1-x}N) + E_{g\alpha} \left[\frac{300^2}{300 + E_{g\beta}} - \frac{T^2}{T + E_{g\beta}} \right] \quad (11)$$

where E_{g300} is given in equation (2) and $E_{g\alpha}$ and $E_{g\beta}$ are material-dependent parameters which are fixed at 9.09×10^{-4} eV K^{-1} and 650 K [15], respectively, for $In_xGa_{1-x}N$ and valid for the whole composition range.

Finally, the minority carrier life time for electrons and holes are taken to be the same (i.e. $\tau_{e,h} = 1$ ns) for $In_xGa_{1-x}N$ over the whole composition range. Auger recombination coefficients for III-N materials shows a large spread in their values and varies from 1×10^{-34} to 5.37×10^{-28} cm^6 s^{-1} obtained from the experimental measurements and theoretical estimations [13, 20, 21]. For the sake of device simulation, their values are fixed at 1.5×10^{-30} cm^6 s^{-1} [13] for electrons and holes for $In_xGa_{1-x}N$.

For cSi (in tandem design), carrier lifetime for electrons and holes was set to 1 ms. Auger coefficients are chosen to be 2.8×10^{-31} and 9.9×10^{-32} cm^6 s^{-1} [15] for electrons and holes respectively, for cSi. Similarly, the bandgap of 1.08 eV [15], permittivity ($\varepsilon/\varepsilon_o$) of 11.8 [15] and affinity (χ) of 4.17 eV [15] are selected for cSi. A low field electron and hole mobility of 1000 and 450 cm^2 V$^{-1} \cdot$ s^{-1} [15] is used for cSi. For device simulation, a set of physical models, which includes bandgap narrowing effect, doping- and temperature-dependent mobility models, Schokly–Read–Hall (SRH) recombination model, and Auger recombination model, and Fermi Dirac statistics [15]
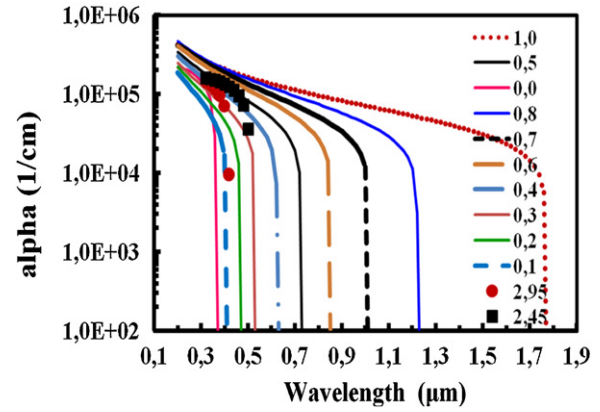

Figure 2. Absorption coefficient as a function of wavelength for different indium content in the InGaN. Points are shown from the best fit curve of experimental data given in [13] for an InGaN bandgap of 2.95 and 2.45 eV.

are implemented. Transport of the carriers is modeled by standard drift-diffusion equations [15]. Defect recombination at the semiconductor heterointerfaces is modeled by the inclusion of a recombination velocity parameter. Transport at the heterointerfaces has been taken into account using the thermionic field emission tunneling model [15]. Simulation data presented here deal with inbuilt TCAD AM1.5 solar spectrum.

3. Results and discussion

Reliable solar cell modeling should be based on accurate and reliable optical and electrical modeling parameters of the device. Hence a prerequisite to solar cell modeling is the use of a photon energy-dependent optical constant in the form of $n(E)$ (see equation (7)) and $k(E)$ values (where $k(E) = \alpha \cdot \lambda/4\pi$ [15], α is absorption coefficient given in equation (1)) of the solar material. Such dispersion relations describing $n(E)$ and $k(E)$ of the III-N network for wide energy gaps are usually unavailable in the commercial TCAD software package [15]. Figure 2 shows the absorption coefficient (calculated by equation (1)) for different indium contents in the InGaN material. Also shown are the experimental data [13] confirming high absorption coefficients in the InGaN material. The absorption coefficients of InGaN are in the order of 10^5 cm^{-1} and drop rapidly below the band edge (absorption is neglected below the bandgap). A very similar shape (both qualitative and quantitative) of the absorption spectra of GaN is also reported by Muth *et al* [17]. Note that this absorption coefficient is 1 order of magnitude higher than that of GaAs (III-V) material, meaning that only 100 nm is sufficient to absorb 63% of light [13, 15].

An energy band diagram under the equilibrium condition of the studied structures is illustrated in figure 3 for (a) SHJ p^+-GaN/n^--InGaN/n^+-InGaN, (b) DHJ p^+-InGaN/n^+-GaN, (c) tandem design with top p^+-GaN/n^--InGaN/n^+-InGaN component cell and p^+-cSi/n^--cSi bottom cell, (d) tandem-graded design based on top component cell of p^+-GaN/graded-InGaN/n^--InGaN/n^+-InGaN and p^+-cSi/n^--cSi bottom cell. A sharp conduction and valence band
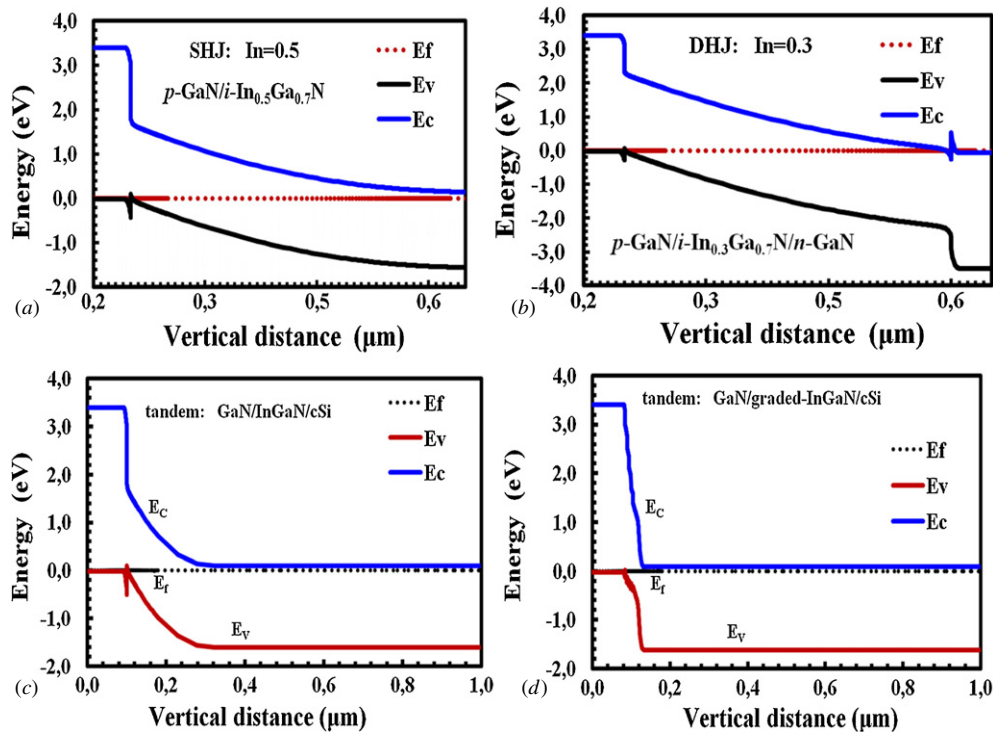
Figure 3. Energy band diagram under equilibrium condition for (*a*) single-heterojunction p^+-GaN/n^--InGaN, (*b*) double-heterojunction p^+-GaN/n^--InGaN/n^+-GaN, (*c*) tandem design with top p^+-GaN/n^--InGaN/n^+-InGaN component cell and p^+-cSi/n^--cSi bottom cell (*d*) tandem-graded design based on top component cell of p^+-GaN/graded-InGaN/n^--InGaN/n^+-InGaN and p^+-cSi/n^--cSi bottom cell. Note that only the top portion of the band diagram of tandem design and tandem-graded design is shown for clarity. Tandem-graded design has eliminated the potential spike appearing in the tandem design (*c*) in the top portion of the band diagram.

offset is visible in the DHJ and SHJ design. Appearance of these band offsets prevents the transport of the photogenerated carriers in the absorber layer from crossing into the respective contacts. Note that only the top portion of the band diagram of tandem design and tandem-graded design is shown for clarity. Tandem-graded design has eliminated the potential spike appearing in the tandem design (c) at the top portion of heterojunction. The grading is employed within 50 nm from the top heterointerface (i.e. p^+-GaN/n^--InGaN) with increasing indium content from 0 to 0.5 (i.e. decreasing bandgap of $In_xGa_{1-x}N$).

Conversion efficiency as a function of indium content for DHJ and SHJ design is plotted in figure 4. Also shown is the efficiency versus absorber thickness for DHJ design. The efficiency increases with indium content, reaches to a maximum value and then sharply drops for larger indium content for SHJ and DHJ design. The efficiency first increases with the increase of the indium content due to the increase in the short-circuit current (decrease in the band gap of the absorber). However, the maximum achievable efficiency point is different for SHJ and DHJ design. This is due to the fact that increasing indium content increases the band offset (i.e. decreases the band gap of InGaN) for the GaN/$In_xGa_{1-x}N$ heterojunction where the conduction band discontinuity (ΔE_c) is larger than the valence band discontinuity (ΔE_v) [13, 14, 16]. A band discontinuity ratio of ΔE_c:$\Delta E_v = 70$:30 [20] is used in the simulation for the GaN/$In_xGa_{1-x}N$ heterojunction. Thus a larger conduction band offset for higher indium content for the DHJ does not allow electrons to pass through the

potential barrier. Note that the SHJ heterojunction does not have any ΔE_c at the n^--InGaN/n^+-InGaN bottom interface. A maximum efficiency of 20% is achieved at indium content of 0.6 ($In_{0.6}Ga_{0.3}N$) for SHJ where the efficiency is limited by the transport of photogenerated holes which cannot surmount the large valence band potential barrier that increases with the indium content. A rapid decrease in the fill factor (hence increasing the series resistance due to large valence band offset) and enhanced recombination of the photogenerated carriers is therefore observed for large indium content beyond 0.6. Similarly, the maximum efficiency for DHJ is achieved at indium content of 0.3 and then decreases sharply because of the large increase in the conduction band offset (i.e. barrier for photogenerated electrons: $\Delta E_c > \Delta E_v$) as earlier said. Predicted by the present simulation, use of the p^+-GaN/n^--InGaN/n^+-GaN (DHJ) structure may therefore be ruled out due to higher conduction band offset (barrier for electrons) which allows us to use only smaller indium content that leads to limited efficiency potential. The situation for SHJ is fairly relaxed where the use of higher indium content is possible due to smaller valence band discontinuity. For fixed indium content, the efficiency increases with the increase of thickness (due to the increase in the short-circuit current) for DHJ as expected and saturates when the thickness reaches to about 1 μm.

Detailed knowledge of the conduction and valence band offsets between InN and GaN is crucial not only to obtain a fundamental understanding of the electronic properties of InGaN alloys but also to obtain reliable design of
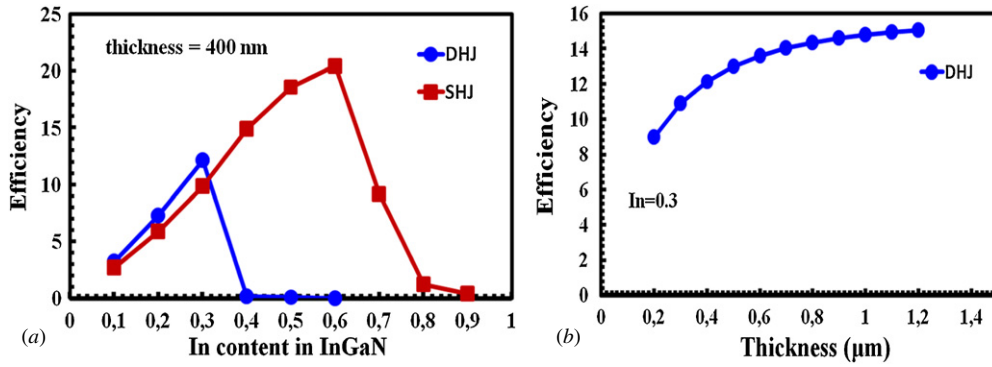
Figure 4. Efficiency as a function of indium content in the InGaN absorber for single (SHJ)- and double (DHJ)-heterojunction design. Also shown is the efficiency versus absorber thickness for double-heterojunction design.
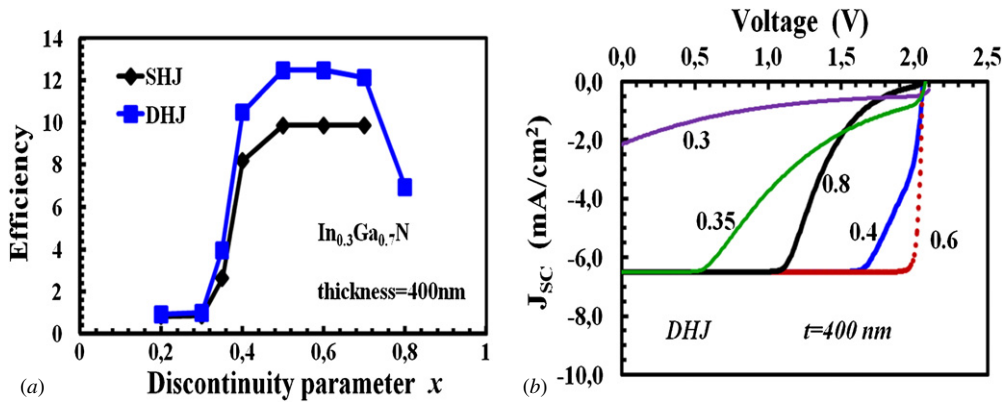

Figure 5. Efficiency as a function of band discontinuity parameter x (where $\Delta E_c = x \cdot \Delta E_g$ and $\Delta E_v = (1-x) \cdot \Delta E_g$ where ΔE_g is the bandgap difference of the two materials) for single (SHJ)- and double-heterojunction (DHJ) devices (a). Also shown is the current–voltage characteristic curve (b) for DHJ design for different band discontinuity parameters.

heterostructure-based InGaN optoelectronic devices. Recent theoretical and experimental findings [20, 22–27] show a large spread in the values of the band offsets for GaN/InN and GaN/InGaN systems. For example, a conduction to valence band offset ratio of $\Delta E_c : \Delta E_v = 61{:}39$ [23], 79:21 [22] 68:32 [24] for the GaN/InN heterojunction has been reported. Similarly, a conduction-to-valence-band offset ratio of $\Delta E_c : \Delta E_v$ of 58:42 [25], 74:26 [26], 62:38 [27] and 70:30 [20] has been presented for the GaN/InGaN system. Note that the indium composition at which the band discontinuity affects the photogenerated carrier collection is determined primarily by the choice of the band offsets values. Figure 5 illustrates the efficiency as a function of the band discontinuity parameter x (where $\Delta E_c = x \cdot \Delta E_g$ and $\Delta E_v = (1 - x) \cdot \Delta E_g$, where ΔE_g is the bandgap difference of the two materials) for the SHJ and DHJ heterojunction devices for an indium content of 0.3 in the $In_{0.3}Ga_{0.7}N$ absorber. A current–voltage characteristic curve is also shown for DHJ design for different discontinuity parameter x indicating the transport behavior of photogenerated carriers at smaller and large values of x. The conversion efficiency increases with the band offsets parameter, attains its maximum value for limited range of the band discontinuity parameter (i.e. $x = 0.5$–0.7) and then decreases for larger values of x for DHJ. For smaller x values, efficiency drops because photogenerated holes cannot surmount the valence band potential barrier and for x

greater than 0.7, the efficiency drops because conduction band discontinuity impedes photogenerated electrons' transport. Compared to SHJ, DHJ predicts higher efficiency for a given discontinuity parameter due to higher V_{OC} of the DHJ. Note that the range of x values where the maximum efficiency is achieved for a given indium content in $In_xGa_{1-x}N$ predicts approximately the same ratio of band offsets ($\Delta E_c : \Delta E_v$) observed by various authors [20, 25, 27].

With the knowledge of indium content and band discontinuity of the GaN/InGaN-based SHJ and DHJ design discussed so far, the use of III-N on silicon (a so called tandem design) provides an interesting low cost and highly efficient design alternative. Tandem-type design using GaN/InGaN top component cell on crystalline silicon will not only provide enhanced spectral coverage but also introduce a natural tunnel junction between the p-Si and n-InGaN, thereby eliminating the need for highly doped regions in conventional multijunction solar cells [10, 12, 14]. A conversion efficiency as a function of indium content for p^+-GaN/n^--$In_xGa_{1-x}N$/n^+-$In_xGa_{1-x}N$/p^+-cSi/n^--cSi tandem design and p^+-GaN/n^--graded-$In_xGa_{1-x}N$/n^--$In_xGa_{1-x}N$/n^+-$In_xGa_{1-x}N$/p^+-cSi/n^--cSi tandem-graded design is presented in figure 6. Current–voltage characteristics for both tandem designs are also shown. A maximum conversion efficiency of as high as 27.0 and 28.7% is obtained using indium content of 0.5 for tandem design
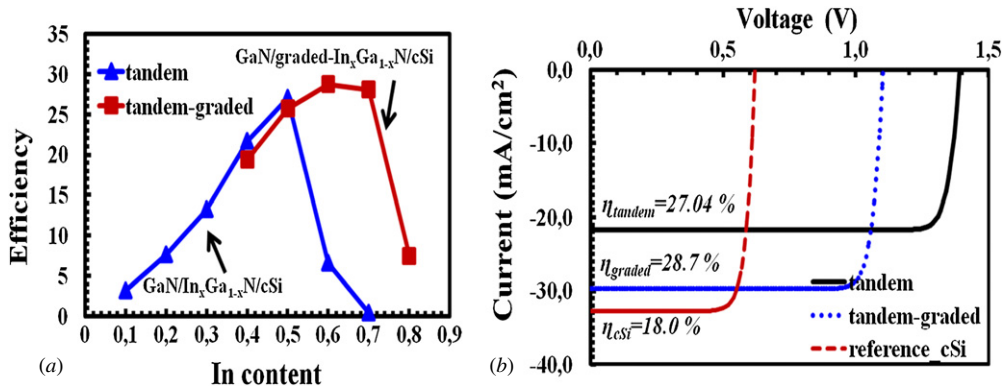
Figure 6. Efficiency as a function of indium content using p^+-GaN/n^--In$_x$Ga$_{1-x}$N/n^+-In$_x$Ga$_{1-x}$N/p^+-cSi/n^--cSi tandem design and p^+-GaN/n^--graded-In$_x$Ga$_{1-x}$N/n^--In$_x$Ga$_{1-x}$N/n^+-In$_x$Ga$_{1-x}$N/p^+-cSi/n^--cSi tandem-graded design (*a*). Also shown is the current–voltage characteristics curve (*b*) for tandem design, tandem-graded design and cSi reference sample. The thickness of crystalline n-silicon (n-cSi) wafer is 200 μm.

(i.e. p^+-GaN/n^--In$_{0.5}$Ga$_{0.5}$N/n^+-In$_{0.5}$Ga$_{0.5}$N/p^+-cSi/n^--cSi) and 0.6 for tandem-graded design (i.e. p^+-GaN/n^--graded-In$_x$Ga$_{1-x}$N/n^--In$_{0.6}$Ga$_{0.4}$N/n^+-In$_{0.6}$Ga$_{0.4}$N/p^+-cSi/n^--cSi), respectively. Compared to tandem design, elimination of valence band discontinuity at the top heterojunction fairly helps to improve the efficiency of tandem-graded design. Since the valence band discontinuity at the top heterojunction is eliminated in tandem design, a higher indium content in the rest of the top InGaN absorber could be incorporated to achieve higher efficiency. These efficiency numbers are comparable to highly efficient (∼30%) GaInP/GaAs-based DHJ cells [28, 29]. A reference design based on p^+-cSi/n^--cSi simulation under identical conditions (i.e. cSi thickness = 200 μm, τ_n/τ_p = 1 ms, wafer n-doping = 1×10^{16} cm^{-3}, electron (hole) mobilities in cSi of 1000 (450) cm^2 V$^{-1}\cdot$s^{-1}) produces an efficiency of just 18%. Since InGaN can be grown on silicon substrate [10, 11, 30], realization of highly efficient and cheap tandem cell presents a new possibility for photovoltaics.

Influence of doping and acceptor traps located at the heterojunction interfaces of semiconductors on conversion efficiency is shown in figure 7. For a given absorber thickness (t = 0.4 μm for DHJ/SHJ), efficiency decreases with the increase of absorber doping (i.e. n-doping in top In$_{0.3}$Ga$_{0.7}$N). Compared to DHJ, a decay in efficiency is more visible for SHJ design at higher doping level. This is explained by the difference in the field profile for SHJ and DHJ design and how it is changed with increasing n-doping in the absorber. For DHJ design, efficiency is hardly affected due to higher built-in electric field (>10^5 V cm^{-1}) presence both at the top and bottom side of the heterojunction which helps to improve the photogenerated carrier collection. So, the photogenerated carriers in the absorber layer are easily transported to the respective side of the device even for higher doping levels for DHJ. The electric field magnitude is higher at the top heterointerface (>10^5 V cm^{-1}) for SHJ device and decays gradually towards the bottom side of the absorber with an approximate magnitude of 3–5 × 10^4 V cm^{-1}. With higher doping level for SHJ design, the built in electric field drops sharply (steep field gradient) close to the top heterojunction and becomes significantly lower in the middle and bottom

side of the absorber (i.e. n^--In$_{0.3}$Ga$_{0.3}$N/n^+-In$_{0.3}$Ga$_{0.3}$N bottom interface) where it attains a field of ∼10^3 V cm^{-1}. Thus transport of the holes (i.e. holes have higher effective masses and lower mobility) generated in the middle and bottom side of the absorber is significantly affected due to very low field presence in the whole InGaN absorber. Looking deeper into the structure, in fact a higher recombination rate is observed as a result of the changed electric field profile due to higher doping. Hence, this causes a decrease in efficiency for SHJ device with higher doping. For tandem-graded design, the influence of top absorber doping on efficiency is significant for higher doping level (>1 × 10^{17} cm^{-3}). Here the top absorber is 1.0 μm. The electric field is higher at the top and bottom heterointerfaces (i.e. ∼10^5 V cm^{-1} at p^+-GaN/n^--InGaN and n^+-InGaN/p^+-cSi) and lower (>10^3 V cm^{-1}) in the middle portion of the absorber for tandem-graded design at smaller doping level. For low absorber n-doping, this field is sufficient for the carrier collection in the top absorber. When the n-doping is increased to a higher level (>1.0 × 10^{17} cm^{-3}), the field profile is severely changed. Now, the field gradient is steeper at the top and bottom heterointerfaces of the top component cell and drop significantly (<1.0^2 V cm^{-1}) over larger portion of the top absorber thickness (approximately 0.8 μm). Thus, transport of the carrier is impeded due to very low field zone presence 'dead field zone' which alternatively leads to higher recombination and hence severe drop in the efficiency is expected for very high doping level. The explanation presented here is consistent with the similar trend observed earlier [31] for n-doped absorber in a-Si:H (hydrogenated amorphous silicon) p–i–n-type solar cells.

The performance of heterojunction solar cells crucially depends on the morphological and electronic properties of the interface [32–34] due to the fact that the interface is located inside the space charge region. Providing a clean and microscopically smooth crystalline silicon (cSi) surface prior to the deposition or growth of dissimilar layers, in order to reduce the defect density D_{it} to a non-detrimental level (below $D_{it} < 10^{11}$ cm^{-2} eV^{-1}) [33] is a prerequisite but challenging process step. At the cSi surface or at the interface of two dissimilar materials, different electronic states in the band gap are present resulting from strained bonds and
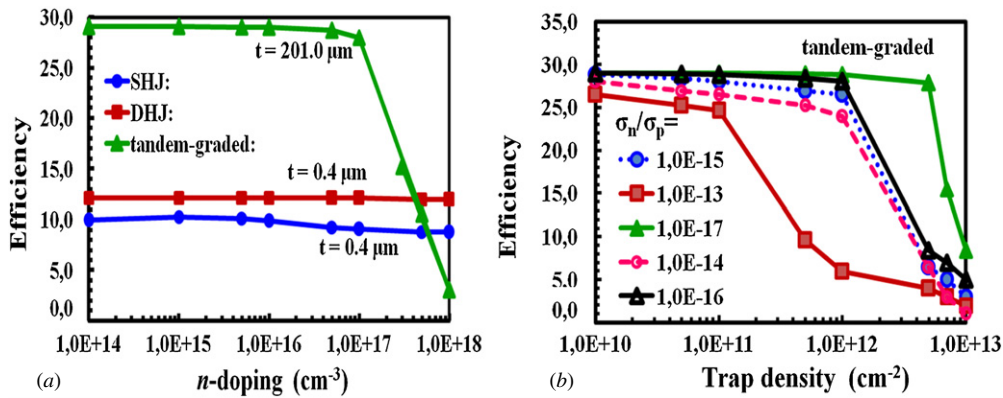
Figure 7. Efficiency as a function of doping (*a*) for different structures and acceptor interface trap density (*b*) for tandem-graded design.

broken/dangling bonds. In addition, a native oxide growing in ambient air when hydrogen and oxygen are present induces further electronic states in the band gap. The issue of the presence of surface states and traps at the interface of the heterojunction arising from the lattice mismatch of Si and GaN/InGaN and the difference of the thermal expansion coefficients of two materials [10, 11, 30, 32] is significant since these interface states or interface traps act as efficient recombination centers and therefore reduce the current density and efficiency potential of solar cells. Interface properties have therefore been studied by introducing acceptor traps (single energy level at 0.5 eV below the conduction band) at the heterointerfaces of the tandem-graded structure. Simulations have been performed by varying acceptor trap density and trap capture cross-section for electrons and holes since both parameters influence the capture and generation rate of the carriers. Figure 7(*b*) presents the efficiency versus acceptor interface trap density with different capture cross-section. The trap density and electron cross-section both significantly degrade the efficiency by reducing the fill factor. The decay in efficiency starts from lower values of the trap density for larger capture cross-section ($\sim 10^{-13}$–10^{-14} cm^2). For smaller capture cross-section ($\sim 10^{-15}$–10^{-17} cm^2), the efficiency degrades rather slowly until 1×10^{12} cm^{-2} is reached and then declines sharply for very large trap density.

With GaN/InGaN-based high temperature applications [32] in mind, temperature dependence performance of SHJ, DHJ heterojunction and tandem-graded design is finally assessed. In general, the temperature dependence of the solar cell performance has been recognized as one of the most important characteristics for determining output power in practical use. Temperature sensitivity of a solar cell depends on the open-circuit voltage of the solar cell, with higher voltage solar cells being less affected by temperature and favourable for obtaining more power in practical use. Earlier, silicon-based HIT cell (i.e. *a*-Si:H/*c*-Si heterojunction) has shown a better voltage temperature coefficient of $-0.33\%/^\circ$C than that of conventional p/n diffused silicon solar cell whose temperature coefficient is $-0.45\%/^\circ$C [33]. A measurement for triple junction InGaP/InGaAs/Ge solar cell shows a temperature coefficient of $-0.24\%/^\circ$C (i.e. -5.89 mV/$^\circ$C) [34]. Recent temperature dependence analysis for *p–i–n*-type 0.3 μm thick homojunction In$_{0.14}$Ga$_{0.86}$N solar cell

shows a drop of V_{OC} (from its room temperature value) of -42% at 200 $^\circ$C and 60% upto 250 $^\circ$C. A severe loss in the V_{OC} is linked not only with the reduction in the bandgap (with increasing temperature) but also material defects and non-optimized device structure has played a key role for this change in V_{OC}. Figure 8 illustrates the simulation analysis of SHJ, DHJ and tandem-graded design for different temperature. A temperature coefficient of -0.15 (-2.7), -0.09 (-1.7) and -0.2 (-2.19)%/$^\circ$C (mV/$^\circ$C) for SHJ, DHJ and tandem-graded design has been obtained reflecting superior temperature behavior to that of silicon or III–V counterparts [33, 34]. Similarly, the temperature coefficient of efficiency (i.e. $\beta = \Delta\eta/\eta\Delta T$ $^\circ$C^{-1}) for SHJ, DHJ and tandem-graded design of -1.72, -0.95, and 2.38×10^{-3} $^\circ$C^{-1}, respectively, has been obtained. These numbers are superior to Si (-4.6×10^{-3} $^\circ$C^{-1}) [35] and double junction GaAs (-2.85×10^{-3} $^\circ$C^{-1}) [35] based solar cells.

Finally, current status of InGaN/GaN-based SHJ or DHJ solar cells on different substrates is presented in table 1. While the conversion efficiency achieved so far for InGaN/GaN cells lies around 1–3% [9–11, 36–40, 42, 43], one of the most serious issues for further improvements of device performance is the difficulty of fabricating thick InGaN films with high crystalline quality and a high InN molar fraction. As the In content increases, the critical thickness of the InGaN layer decreases to maintain epitaxial quality [36, 37, 42]. Therefore, further reducing the dislocation density for thick In-rich InGaN layers is critical for overall conversion efficiency improvement. Simulated data show a fair comparison with experimental *p–i–n*-type DHJ InGaN/GaN solar cells [39, 40]. More interestingly, the modeled value for the bandgap (i.e. 2.982 eV from equation (2)) reflects very closely that of the experimental value (i.e. 3.02 eV) for In$_{0.11}$Ga$_{0.89}$N material [39]. Similarly, a reasonable match for the bandgap of In$_x$Ga$_{1-x}$N for other indium contents is also obvious from modeled (experimental: [9]) values (e.g. 2.647(2.64), 2.3(2.63) and 2.0(2.1) eV for In content of 0.2, 0.3 and 0.4 respectively). While the modeled absorption coefficient for InGaN material (i.e. $\sim 10^5$ cm^{-1} equation (1) and figure 2) lies close to that of the experimental one, a better agreement with the experimental data may further be achieved by fine tuning the defect density, and recombination parameters at the heterointerfaces which is
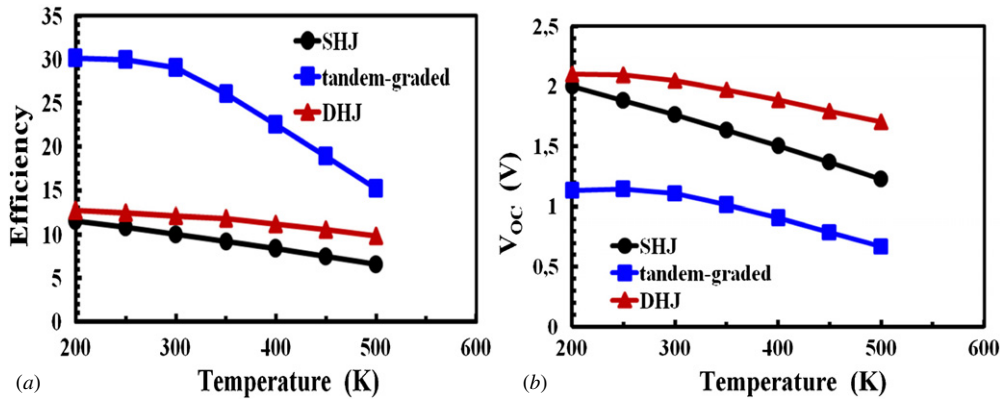
Figure 8. Efficiency (*a*) and open-circuit voltage (*b*) as a function of temperature for single-heterojunction (SHJ), double-heterojunction (DHJ) and tandem-graded design.

Table 1. Current status of InGaN/GaN-based solar cells. Also shown are the simulated data from this work for comparison with *p–i–n*-type DHJ solar cells.

		Experimental				Simulated			
		V_{OC}	J_{SC}	FF	□	V_{OC}	J_{SC}	FF	□
References	Device type	V	mA cm^{-2}	%	%	V	mA cm^{-2}	%	%
[36] 2011	*p-i-n* In$_{0.12}$Ga$_{0.88}$N/GaN	1.25	0.70	65.62	2.56	–	–	–	–
	p-i-n In$_{0.02}$Ga$_{0.98}$N/GaN	2.06	0.54	69.3	3.37	–	–	–	–
[42] 2011	In$_{0.2}$Ga$_{0.8}$N/GaN grown on a Si substrate	1.0	–	–	–	–	–	–	–
[43] 2011	InGaN/GaN	1.89	1.06	79	–	–	–	–	–
[9] 2009	MQW In$_{0.3}$Ga$_{0.7}$N/GaN with 8 periods of nGaN(3 nm)/GaN(8 nm)	2.0	1.50	60	–	–	–	–	–
[37] 2011	In$_{0.17}$Ga$_{0.83}$N/In$_{0.07}$Ga$_{0.93}$N of 3 nm/0.6 nm with 50 pairs superlattce structure on a GaN substrate	1.78	3.08	70.8	2.50	–	–	–	–
[38] 2009	*p-i-n* In$_{0.1}$Ga$_{0.9}$N/GaN DHJ grown on a sapphire substrate	2.09	0.52	73.0	0.80	–	–	–	–
[39] 2010	*p-i-n* In$_{0.11}$Ga$_{0.89}$N/GaN DHJ grown on a GaN substrate	2.01	0.644	79.8	1.00	2.0	1.05	85	1.30
[40] 2011	*p–i–n*-type DHJ of GaN/In$_{0.17}$Ga$_{0.83}$N/GaN on a sapphire substrate	2.08	0.74	70.4	1.09	2.02	1.15	86	1.42

justifiable for the InGaN/GaN system. In fact, an enhancement in the current density and fill factor is linked with the reduction in the dislocation densities and improvement in the interface quality [37, 39, 40]. Note that the modeling parameters used for crystalline silicon material (special for tandem design) have already reflected the realistic conversion efficiency of *a*-Si/cSi HIT cells [41] and hence justifying the predicted efficiency potential of InGaN/GaN/Si tandem design presented in this study.

4. Conclusions

A theoretical efficiency potential of three structures namely SHJ (p^+-GaN/n^--InGaN/n^+-InGaN), DHJ (p^+-GaN/n^--InGaN/n^+-GaN) and tandem-graded design (p^+-GaN/n^--graded-InGaN/n^--InGaN/n^+-InGaN/p^+-cSi/n^--cSi) is investigated using two-dimensional numerical simulation. A conversion efficiency of 27% is achieved using a 1.0 μm thick In$_{0.5}$Ga$_{0.5}$N absorber of the top cell over a 200 μm thick crystalline silicon (cSi) bottom cell for the double junction GaN/InGaN/cSi tandem design. With grading the In$_x$Ga$_{1-x}$N absorber layer close to the top heterointerface (*p*-GaN/n^--In$_x$Ga$_{1-x}$N) of the top component cell, the conversion efficiency is further improved to 29.0% for tandem-graded design. For a given indium content in the top In$_x$Ga$_{1-x}$N absorber, a maximum conversion efficiency is obtained when the band discontinuity ratio (i.e. ΔE_C:ΔE_V) is set to 0.65:0.35. While a

moderate *n* doping (up to 5 $\times$ 10^{16} cm^{-3}) in the InGaN absorber does not influence the efficiency, an interface trap density over 5 $\times$ 10^{11} cm^{-2} and large trap cross-section (exceeding 1 $\times$ 10^{-14} cm^2) have notorious impact on the conversion efficiency. Numerical simulations further predict a temperature coefficient for the open-circuit voltage (efficiency) of -0.15 (-1.72×10^{-3} °C^{-1}), -0.09 (-0.95×10^{-3} °C^{-1}) and -0.2 (-2.38×10^{-3} °C^{-1})%/°C for SHJ, DHJ and tandem-graded design.

References

[1] Cho C, Lee J, Lee S, Han S, Park T, Kim J, Kim Y and Park S 2010 Improvement of light output power of InGaN/GaN light-emitting diode by lateral epitaxial overgrowth using pyramidal-shaped SiO *Opt. Express* **18** 1462–8

[2] Kikuchi A, Tadaa M, Miwaa K and Kishino K 2006 Growth and characterization of InGaN/GaN nanocolumn LED *Proc. SPIE* **6129** 612905–1

[3] Dadgar A, Hums C, Diez A, Schulze F, Bläsing J and Krost A 2006 Epitaxy of GaN LEDs on large substrates: Si or sapphire? *Proc. of SPIE* **6355** 63550R–1

[4] Wang Q, Savage S, Persson S, Noharet B, Junique S and Andersson J 2009 Multiple functional UV devices based on III-nitride quantum wells for biological warfare agent detection *Proc. SPIE* **7216** 721627–1

[5] Chiou Y, Su Y, Chang S, Gong J, Lin Y, Liu S and Chang C 2003 High detectivity InGaN–GaN multiquantum well p–n junction photodiodes *IEEE J. Quantum Electron.* **39** 681–5

[6] Green M A, Emery K, Hisikawa Y and Warta W 2008 Solar cell efficiency tables (Version 31) *Prog. Photovoltaics* **16** 61–7

[7] King R R *et al* 2009 Band-gap engineering architectures for high efficiency multijunction concentrator solar cells *24th Eur. Photovoltaic Solar energy Conf.* pp 55–61

[8] Pryce I M, Koleske D D, Fischer A J and Atwater H A 2010 Plasmonic nanoparticle enhanced photocurrent in GaN/InGaN/GaN quantum well solar cells *Appl. Phys. Lett.* **96** 153501

[9] Dahal R, Pantha B, Li J, Lin J Y and Jiang H X 2009 InGaN/GaN multiple quantum well solar cells with long wavelengths *Appl. Phys. Lett.* **94** 063505

[10] Reichertz L A, Gherasoiu I, Yu K M, Kao V M, Walukiewicz W and Ager J W 2009 Demonstration of a III-nitride/Silicon Tandem Solar Cell *Appl. Phys. Express* **2** 122202

[11] Liou B W 2009 High photovoltaic efficiency of $In_xGa_{1-x}N$/Gas-based solar cells with a multiple-quantum-well structure on SiCN/Si(111) substrates *Japan. J. Appl. Phys.* **48** 072201

[12] Hsu L and Walukiewicz W 2008 Modeling of InGaN/Si tandem solar cells *J. Appl. Phys.* **104** 024507

[13] Jani O K 2008 Development of wide-band gap InGaN solar cells for high-efficiency photovoltaics *PhD Thesis* Georgia Institute of Technology August

[14] Brown G F, Ager J W, Walukiewicz W and Wua J 2010 Finite element simulations of compositionally graded InGaN solar cells *Sol. Energy Mater. Sol. Cells* **94** 478–83

[15] Silvaco Data System Inc 2009 *Atlas User Manual* Ver 5.15.31.C

[16] Wu J and Walukiewicz W 2003 Band gaps of InN and group III nitride alloys *Superlattices Microstruct.* **34** 63–75

[17] Muth J F, Lee J H, Shmagin I K, Kolbas R M, Casey H C, Keller B P, Mishra U K and DenBaars S P 1997 Absorption coefficient, energy gap, exciton binding energy, and recombination lifetime of GaN obtained from transmission measurements *Appl. Phys. Lett.* **71** 2572–4

[18] Farahmand M, Garetto C, Bellotti E, Brennan K F, Goano M, Ghillino E, Ghione G, Albrecht J D and Ruden P P 2001 Monte Carlo simulation of electron transport in the III-nitride Wurtzite phase materials system: Binaries and Ternaries *IEEE. Trans. Electron Devices* **48** 535–42

[19] Mnatsakanov T T, Levinshtein M E, Pmortseva L I, Yurkov S N, Simin G S and Khan M A 2003 Carrier mobility model for GaN *Solid-State Electron.* **47** 111–5

[20] Piprek J and Nakamura S 2002 Physics of high-power InGaN/GaN lasers *IEEE Proc.-Optoelectron.* **149** 145–51

[21] Yen S H, Tsai M C, Tsai M-L, Shen Y-J, Hsu T-C and Kuo Y-K 2009 Theoretical investigation of Auger recombination on internal quantum efficiency of blue light-emitting diodes *Appl. Phys. A* **97** 705–8

[22] King P D C, Veal T D, Kendrick C E, Bailey L R, Durbin S M and McConville C F 2008 InN/GaN valence band offset: High-resolution x-ray photoemission spectroscopy measurements *Phys. Rev.* B **78** 033308

[23] Wang K A, Lian C, Su N and Jena D 2007 Conduction band offset at the InN/GaN heterojunction *Appl. Phys. Lett.* **91** 232117

[24] Wei S H and Zunger A 1996 Valence band splittings and band offsets of AlN, GaN, and InN *Appl. Phys. Lett.* **69** 2719

[25] Zhang H, Miller E J, Yu E T, Poblenz C and Speck J S 2004 Measurement of polarization charge and conduction-band offset at $In_xGa_{1-x}N$/GaN heterojunction interfaces *Appl. Phys. Lett.* **84 23** 4644

[26] Makimoto T, Kumakura K, Nishida T and Kobayashi N 2002 Valence-band discontinuities between InGaN and GaN Evaluated by capacitance-voltage characteristics of p-InGaN/n-GaN diodes *J. Electron. Mater.* **31** 313–5

[27] Manz C, Kunzer M, Obloh H, Ramakrishnan A and Kaufmann U 1999 $In_xGa_{1-x}N$/GaN band offsets as inferred from the deep, yellow-red emission band in $In_xGa_{1-x}N$ *Appl. Phys. Lett.* **74** 3993

[28] Takamoto T, Agui T, Ikeda E and Kurit H 2001 High-efficiency InGaP/$In_{0.01}Ga_{0.99}$As tandem solar cells lattice-matched to Ge substrates *Sol. Energy Mater. Sol. Cells* **66** 511–6

[29] Takamoto T, Ikeda E, Kurita H and Ohmori M 1997 Over 30% efficient InGaP/GaAs tandem solar cells *Appl. Phys. Lett.* **70** 381–383

[30] Jampana B, Xu T, Melton A, Jamil M, Opila R, Honsberg C and Ferguson I 2010 Realization of InGaN solar cells on (111) silicon substrate *35th IEEE PVSC (Photovoltaic Specialist Conf.)* pp 457–60

[31] Prentice J 2000 Computer simulation of the effect of phosphorus doping of the i-layer in a thin film a-Si:H p-i-n solar cell *Sol. Energy Mater. Sol. Cells* **61** 287–300

[32] Boney C, Hernandez I, Pillai R, Starikov D and Bensaoula A 2010 InGaN devices for high temperature photovoltaic applications *35th IEEE PVSC (Photovoltaic Specialist Conf.)* pp 2522–7

[33] Taguchi M, Terakawa A, Maruyama E and Tanaka M 2005 Obtaining a higher V_{OC} in HIT cells *Prog. Photovolt. Res.* **13** 481–8

[34] Ota Y, Sakurada Y and Mishioka K 2010 Temperature characteristics analysis of InGaP/InGaAs/Ge triple junction solar cell under concentrated light using spice diode model *35th IEEE PVSC (Photovoltaic Specialist Conf.)* pp 2093–6

[35] Markvart T and Castafier L 2003 *Practical Handbook of Photovoltaics: Fundamentals and Applications* Part IID space and concentrator cells (Amsterdam: Elsevier)

[36] Cai X-M, Zeng S-W, Li X, Zhang J Y, Lin S, Ling A-K, Chen M, Liu W-J, Wu S X and Zhang B P 2011 Dependence of the light property of InGaN p-i-n solar cells on the light concentration and temperature *IEEE Trans. Electron Device* **58** 3905–11

[37] Kuwahara Y *et al* 2011 GaInN-based solar cells using strained layer GaInN/GaInN superlattice active layer on freestanding GaN substrate *Appl. Phys. Express* **4** 021001

[38] Horng R H, Lin S T, Tsai Y L, Chu M T, Liao W Y, Wu M H, Lin R M and Lu Y C 2009 Improved conversion efficiency of GaN/InGaN thin-film solar cell *IEEE. Electron Device. Letts.* **30** 724–7

[39] Shim J P, Jeon S R, Jeong Y K and Lee D S 2010 Improved efficiency by using transparent contact layers in InGaN-based p-i-n solar cells *IEEE. Electron, Device. Letts.* **31** 1140–2

[40] Chu M T, Liao W Y, Horng R H, Tsai T Y, Wu T B, Liu S P, Wu M H and Lin R M 2011 Growth and characterization of p-InGaN/i-InGaN/n-GaN double heterojunction solar cells on patterned sapphire substrates *IEEE. Electron Device. Letts.* **32** 922–4

[41] Nawaz M 2010 Design analysis of *a*-Si/*c*-Si HIT solar cells *Adv. Sci. Technol.* **74** 131–6

[42] Gherasoiu I, Reichertz L A, Yu K M, Ager J W, Kao V M and Walukiewicz W 2011 Photovoltaic action from $In_xGa_{1-x}N$ *p–n* junctions with *x* > 2 grown over silicon *Phys. Status Solidi* **8** 2466–8

[43] Matioli E *et al* 2011 High internal and external quantum efficiency InGaN/GaN solar cells *Appl. Phys. Lett.* **98** 021102